Journal Pre-proof

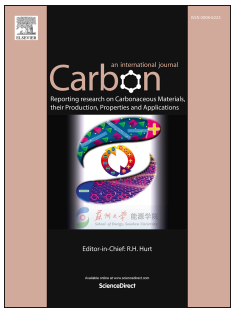

Sub-second Synthesis of Graphite Foam Anchored Atomically Dispersed Ni Atoms: Axial Phosphate Coordination for Improved Electrocatalytic Water Oxidation

Hanbo Li, Duan Yan, Kun Feng, Wei Zhang, Xiaoxin Lv, Jun Zhong, Jiujun Deng

PII: S0008-6223(25)00436-1

DOI: https://doi.org/10.1016/j.carbon.2025.120420

Reference: CARBON 120420

To appear in: *Carbon*

Received Date: 3 March 2025

Revised Date: 4 May 2025

Accepted Date: 11 May 2025

Please cite this article as: H. Li, D. Yan, K. Feng, W. Zhang, X. Lv, J. Zhong, J. Deng, Sub-second Synthesis of Graphite Foam Anchored Atomically Dispersed Ni Atoms: Axial Phosphate Coordination for Improved Electrocatalytic Water Oxidation, *Carbon*, https://doi.org/10.1016/j.carbon.2025.120420.

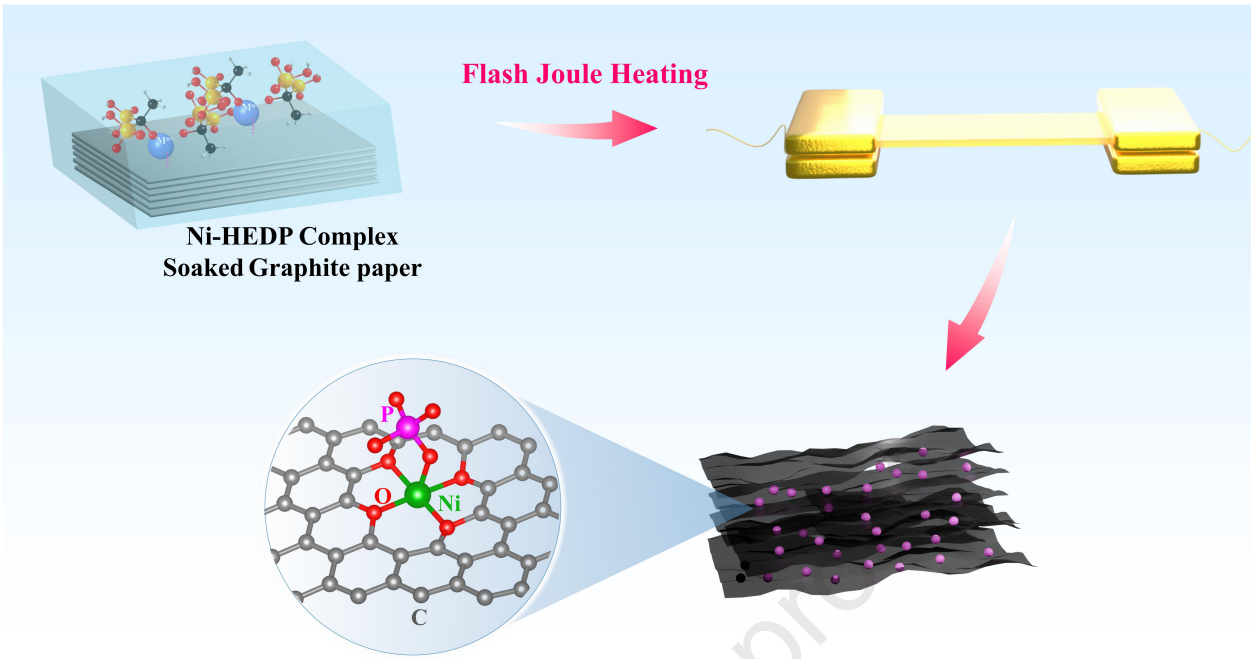

Dispersed Ni Atoms: Axial Phosphate Coordination for Improved Electrocatalytic Water Oxidation

Hanbo Li,[a] Duan Yan,[a] Kun Feng,[b] Wei Zhang, [a] Xiaoxin Lv,[a] Jun Zhong,*[b] and Jiujun Deng*[a]*

[a] Institute for Energy Research, Automotive Engineering Research Institute, Jiangsu University, Zhenjiang 212013, China

[b] Institute of Functional Nano and Soft Materials Laboratory (FUNSOM), Jiangsu Key Laboratory for Carbon-Based Functional Materials & Devices, Soochow University, Suzhou 215123, China

*Corresponding Authors: xxlv@ujs.edu.cn; jzhong@suda.edu.cn; jjDeng@ujs.edu.cn

ABSTRACT: The fabrication of self-supported atomically dispersed catalysts for efficient oxygen evolution reactions (OER) through industrial-scale production remains a significant challenge. In this study, we present a cost-effective method for rapidly synthesizing a self-supporting electrode composed of three-dimensional (3D) graphite foam and axial phosphate-coordinated atomically dispersed Ni atoms, using a wet-interfacial flash Joule heating approach within just 400 milliseconds. It reveals that the high conductivity and large surface area of graphite foam could effectively facilitate electron and proton transport during the OER process. Additionally, the axially coordinated phosphate ligand on the atomically dispersed Ni site could induce an in-situ reconstruction into isolated Ni-OH sites and small $Ni(OH)_2$ clusters during the activation process, further accelerating the OER kinetics. Eventually, the resulting electrode achieves a low overpotential of 250 mV to reach a current density of 10 mA cm^{-2} and remarkable long-term durability. This study offers a novel, rapid, and cost-effective pathway for designing self-supporting electrodes anchored with atomically dispersed catalysts toward an efficient OER process.

KEYWORDS: Self-supporting, Graphite foam, Atomically dispersed catalysts, Axial coordination, Water oxidation

1. Introduction

Electrocatalytic water splitting using renewable energy sources has been considered a green and sustainable approach for hydrogen production [1-5]. In comparison to the hydrogen evolution reaction (HER) at the cathode, the oxygen evolution reaction (OER) that occurred at the anode involves a complex proton-coupled electron transfer, making it a bottleneck in the overall water splitting reaction [1-5]. As a result, recent advancements focus on the development of efficient OER electrocatalysts with accelerated kinetics and lowered overpotential [1-5]. Transition metal-based electrocatalysts as promising candidates have been widely exploited owing to their high abundance, cost-effectiveness, environmental friendliness, and durability [6,7]. Notably, transition metal-based atomically dispersed catalysts (TM-ADCs, including single-atoms, double-atoms, and clusters) are emerging as a new frontier on account of exceptional OER activity resulting from maximum metal atom utilization, tunable coordination environments, and uniform active sites [8-10].

Typically, TM-ADCs are produced in powder and require polymer binders such as Nafion to coat them onto conductive supports (carbon cloth, carbon paper, etc.) for use as the working electrode [11,12]. Unfortunately, this approach suffers from critical drawbacks, such as the burying of active sites, inadequate contact with the electrolyte solution, and restricted transport of reactants and products, seriously degrading the OER performance [13-15]. Constructing self-supporting electrodes by anchoring TM-ADCs onto three-dimensional (3D) carbon-based substrates (e.g., graphene aerogel, graphite foam, and carbon fibers) has been proven an effective strategy [13-15]. These substrates typically possess large specific surface area, high porosity, excellent conductivity, and thermal stability, which can not only prevent the atomically dispersed metal sites from aggregation but also facilitate mass/electron transport, thereby greatly improving OER activity and stability [13-15]. In addition to substrate characteristics, the electrocatalytic performance of TM-ADCs has also been drastically affected by their electronic structure, specifically the coordination environment [16-20].

Recently, axial coordination engineering has emerged as a novel and accessible approach to tuning both geometric and electronic structures of TM-ADCs, garnering increasing attention [16-20]. It has been demonstrated that the axial coordination could intentionally break the planar symmetry of atomically dispersed metal atoms via adding ligands in the axial direction, thus substantially boosting their electrocatalytic OER performance [16,17]. Up to date, a variety of ligands including N-containing ligands, O-containing ligands, and halogen-containing ligands (Cl, Br, I, etc.) have been explored [18-20].

Nevertheless, fabricating self-supporting TM-ADCs through a facile, cost-effective, and environmentally friendly route remains challenging. On one hand, 3D carbon-based substrates are generally produced through hazardous, expensive, and complex synthetic methods [21-24]. On the other hand, high-temperature pyrolysis is a highly feasible pathway for the anchoring of TM-ADCs but is time-consuming and leads to significant aggregation of metal sites [25,26]. More importantly, the precise control of the axial structure of TM-ADCs at elevated temperatures has also been a challenge due to the complicated reaction mechanisms [15]. Therefore, it is highly desirable to develop a facile and efficient method for the construction of 3D carbon substrate-supported and axially coordinated TM-ADCs. In this regard, the flash Joule heating technique has emerged as a promising alternative by achieving rapid heating/quenching rates (10^3-10^5 K s^{-1}), which not only effectively prevents metal atom agglomeration to produce atomical dispersed catalysts but also significantly reduces energy consumption and simplifies the process by minimizing operation time [26-32].

In this study, we present an ultrafast and efficient synthesis for a self-supporting electrode constructed by graphite foam and axial phosphate-coordinated atomically dispersed Ni atoms (labeled as GF/NiSA-P) through a wet-interfacial flash Joule heating approach. By subjecting commercial graphite paper (CGP) pre-impregnated with the Ni-HEDP complex solution to an instantaneous heating/quenching process of approximately 400 milliseconds, carbothermal shock, water evaporation, and CO_2 release induce a rapid expansion of CGP into a 3D graphite foam consisting of multiple graphene layers. Concurrently, the decomposition of the Ni-HEDP complex generates oxidized carbon quantum dots on the graphene surface, which not only further increase the surface area of graphite foam but also act as anchor sites to ensure the

stable atomically dispersion of Ni sites that axially coordinate with the phosphate ligand. Electrochemical measurements show that the high conductivity and the large surface area of graphite foam effectively facilitate electron/proton transport in the OER process. Moreover, it has unraveled an in-situ reconstruction of the axially coordinated phosphate ligand into isolated Ni-OH sites and small $Ni(OH)_2$ clusters during the cyclic voltammetry (CV) activation, which then acts as the real active sites for catalyzing the OER. Consequently, benefiting from the synergistic effects, the GF/NiSA-P electrode exhibits a low overpotential of 250 mV to reach a current density of 10 mA cm^{-2} and remarkable long-term durability in an alkaline electrolyte. This study provides a novel, ultrafast, and cost-effective pathway for the ratio design of self-supporting electrodes anchored with atomically dispersed catalysts toward an efficient OER process.

2. Experimental section

2.1 Sample preparation. For the synthesis of GF/NiSA-P sample, Ni-HEDP complex aqueous solution containing 0.5 M hydroxyethylidene diphosphonic acid (HEDP, Shanghai Macklin Biochemical Co., Ltd. China) and 0.05 M $NiCl_2 \cdot 6H_2O$ (Sinopharm Chemical Reagent Co., Ltd.) was first prepared. Then, a piece of commercial graphite paper (10 × 2.5× 0.02 cm, Beijing Jinglong Tetan Co., Ltd, China) was immersed in Ni-HEDP complex solution and kept for 24 hours. After soaking, the graphite paper was taken out and wiped to remove residual solution from the surface. Then, the pre-soaked graphite paper was connected to the electrical contacts of the flash Joule heating equipment (Hefei In-situ High-tech Co., Ltd. China) and after a rapid heating treatment (electrical parameters: current density of 130 A, duration time of 0.5 s, achieved temperature is about 930 K), the GF/NiSA-P electrode was fabricated, as shown in Figure S1. With the same procedures, the GF-P and GF/Ni samples have also been synthesized by immersing commercial graphite paper in an aqueous solution that only contains HEDP and $NiCl_2 \cdot 6H_2O$, respectively. The GF/Ni-P-dry sample has also been prepared through the same processes as those of GF/NiSA-P except that thoroughly drying the Ni-HEDP complex solution-soaked graphite paper at 60 °C for overnight in a vacuum oven. The commercial RuO_2 electrode was prepared by dispersing 2

mg of the commercial RuO_2 powder (Innochem, 99%) in a mixture of 1 μL of Nafion (5 wt. %) solution and 200 μL of ethanol using an ultrasonic process for 30 min. The resulting homogenous catalyst ink was then pipetted onto commercial graphite paper (1 × 2 cm).

2.2 Structural Characterization. The morphologies of as-obtained samples were characterized by scanning electron microscope (SEM, FEI, Quanta FEG 250) and transmission electron microscopy (TEM, JEOL Ltd, JEM-2100F). The high-angle annular dark field (HAADF) scanning TEM (STEM) images were collected using JEM-ARM300F. The electronic structure was characterized using X-ray photoelectron spectroscopy (XPS, Shimadzu, AXIS-Ultra DLD), and the C 1s peak at 284.8 eV was adopted as an internal standard. X-ray diffraction (XRD) patterns of all the samples were collected using Shimadzu, XRD 6100 with Cu Kα in the range of 10-90°. Raman characterizations were conducted on Horiba, LabRAM HR Evolution. X-ray absorption spectroscopy (XAS) measurements at C K-edge, O K-edge, P L-edge, and Ni L-edge were performed at National Synchrotron Radiation Laboratory (NSRL, Beamlines MCD-A and MCD-B (Soochow Beamline for Energy Materials)). XAS characterizations at Ni K-edge were conducted at the Shanghai Synchrotron Radiation Facility (SSRF, 11B).

2.3 Electrochemical measurements. All electrochemical measurements were performed on a CHI 660E electrochemical workstation with a three-electrodes system, where the as-obtained samples (1 cm × 1 cm) as working electrodes, the Hg/HgO electrode (1.0 M KOH) was the reference electrode, and the platinum sheet was the counter electrode. 1.0 M KOH aqueous solution (pH=14) was used as the electrolyte. The applied potentials were calibrated using the reversible hydrogen electrode (RHE) potential according to the equation:

$$E_{RHE} = E_{Hg/HgO} + 0.0592 \times pH + 0.098 \quad (1)$$

Before the electrochemical measurements, the as-resulted electrodes were activated by performing cyclic voltammetry (CV) scans in 1.0 M KOH solution (100 mV s^{-1}, 20 scans, potential window 0.3-0.9 V vs Hg/HgO) and all linear sweep voltammetry (LSV) curves were recorded at a scan rate of 5 mV s^{-1} with iR correction (90%). R represents the series resistance measured by Electrochemical impedance spectroscopy (EIS). EIS measurements were

conducted at an open circuit potential with an AC amplitude of 5 mV in the range of 0.1

1×10^5 Hz. The overpotential (η) was calculated using the equation:

$$\eta = E_{RHE} - 1.23 \quad (2)$$

The electrochemical double layer capacitance (C_{dl}) was determined by the CV scans that were performed at 0.20 - 0.30 V vs Hg/HgO with various scan rates (10, 20, 40, 60, 80, and 100 mV s^{-1}).

3. Results and discussion

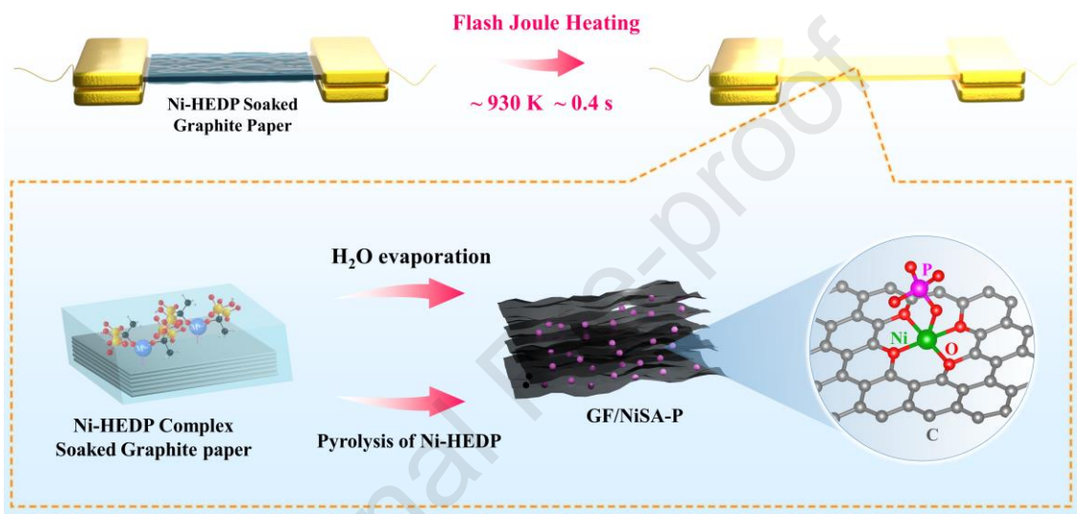

Figure 1. Schematic synthesis process of GF/NiSA-P electrode via the wet-interfacial flash Joule heating strategy.

Commonly, commercial graphite paper (CGP) is comprised of interlaced graphite thin layers that are parallel to the surface, enabling the fabrication of graphite foam through exfoliation methods such as electrochemical exfoliation and liquid nitrogen exfoliation [22-24]. Moreover, CGP has shown a significant flash Joule heating effect [32-34]. In such ends, upon applying a pulse current to CGP pre-soaked with Ni-HEDP complex solution, the resulting instantaneous carbothermal shock (a high temperature of ~930 K is achieved in about 160 ms, Figure S1), the evaporation of water molecules, and the release of CO_2 from the decomposition of Ni-HEDP complex could induce a rapid and substantial expansion of CGP into 3D graphite foam (Figure 1). As displayed in Figure S2 and Figure 2, photographs reveal that after the flash Joule heating treatment, the thickness of CGP drastically increases by 30 times, from 0.2 mm to approximately 6 mm for the resulting GF/NiSA-P electrode. Concurrently, the initially smooth

and flat surface of CGP turns into a rough and porous texture. Figure 2 also illustrates the scanning electron microscopy (SEM) images of CGP and the resulting GF/NiSA-P samples. Different from the dense structure of CGP, the GF/NiSA-P electrode exhibits worm-like strips composed of largely crumpled graphene-liked nanosheets, accompanied by abundant micro-voids. Given that the porous and void structure could increase the contact area between the electrode and the electrolyte and meanwhile provide effective pathways for mass transport, the OER activity of the GF/NiSA-P electrode could thusly be greatly promoted.

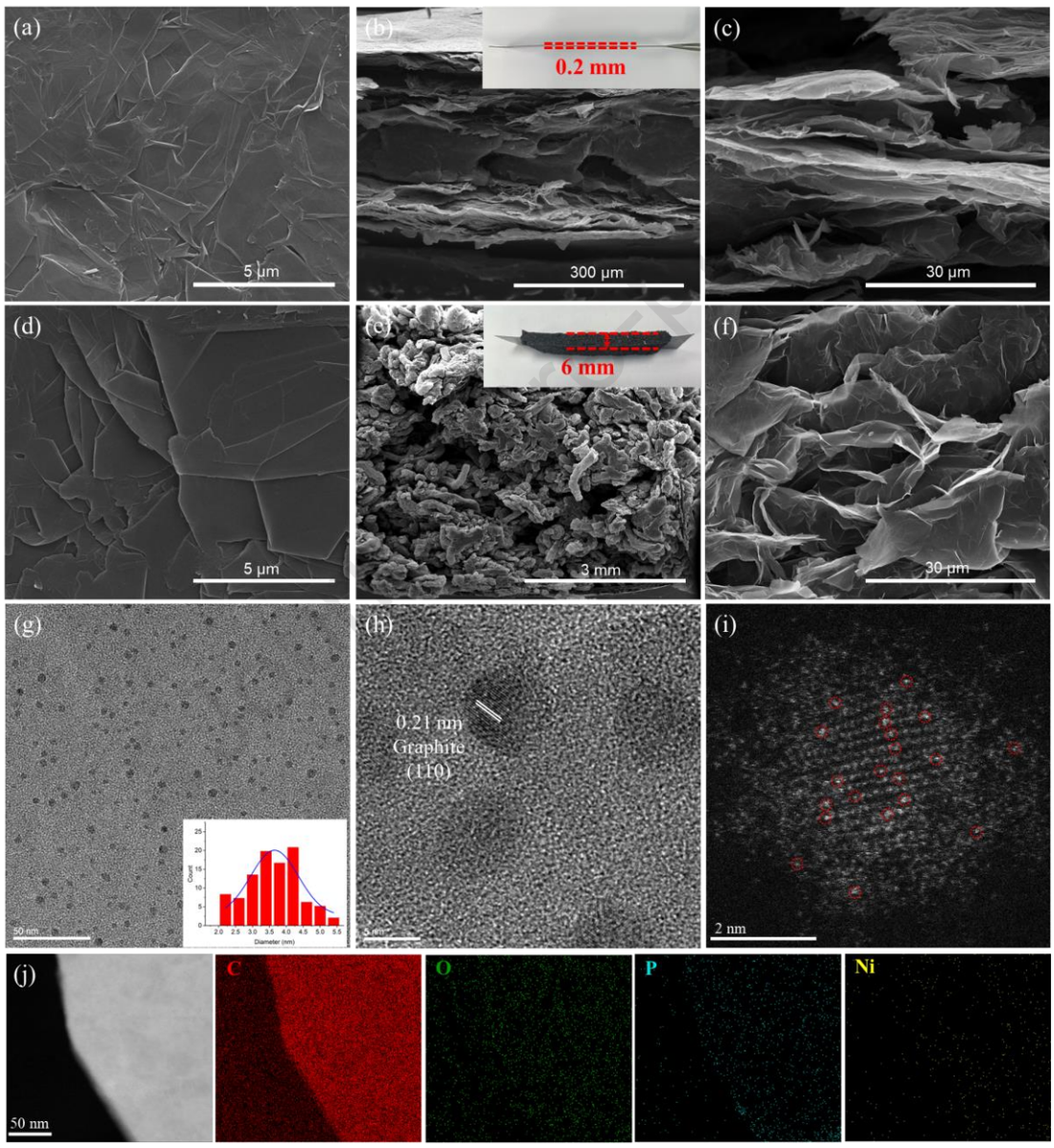

Figure 2. Top-view SEM images, cross-sectional SEM images, and magnified cross-sectional SEM images of CGP (a, b, c) and GF/NiSA-P (d, e, f) samples, respectively; HRTEM images (g, h), HAADF-STEM image (i), and (j) element mappings of GF/NiSA-P sample.

It is well documented that the rapid heating/quenching characteristics of flash joule heating are favorable for creating atomic-level dispersed catalysts by preventing the aggregation of

metal precursors during pyrolysis [26-30]. Therefore, it is reasonable to deduce that the generation of atomically dispersed Ni atoms in the concurrent construction of 3D graphite foam through the ultrafast decomposition of the Ni-HEDP complex. To verify it, high-resolution transmission electron micrograph (HRTEM) and high-angle annular dark-field scanning TEM (HAADF-STEM) characterizations were performed to acquire more information on the subtle morphology of the GF/NiSA-P electrode. As displayed in Figure S3, TEM images of the GF/NiSA-P electrode reveal the morphology of graphene-like nanosheets with large surface area, further confirming the construction of 3D graphite foam via the wet-interfacial flash Joule heating treatment. HRTEM images of the GF/NiSA-P electrode in Figure 2g and Figure 2h highlight a uniform distribution of carbon quantum dots (CQDs) on the surface of graphene-like nanosheets, with an average size of 3.6 nm. The clear lattice fringes of 0.21 nm match well with the (100) facet of graphite [35]. The surface decoration of CQDs has been observed in HRTEM images of the GF-P sample but not on the surface of CGP, as demonstrated in Figure S4, manifesting that the CQDs generation can be attributed to the pyrolysis of HEDP during the flash Joule heating processes. Figure 2i shows the HAADF-STEM image of the GF/NiSA-P electrode, which demonstrates bright spots anchored on the surface of CQDs, representing the atomically dispersed Ni atoms. Figure 2j depicts the energy dispersive X-ray spectroscopy (EDX) mapping of the GF/NiSA-P electrode, revealing a homogeneous distribution of C, O, P, and Ni elements throughout the architecture. These observations clearly indicate the successful synthesis of a self-supporting electrode featuring 3D graphite foam, CQDs, and atomically dispersed Ni atoms through the flash Joule heating treatment.

Figure S5 shows the XRD patterns of the resulting samples, in which intense diffraction peaks around 26° are observed, corresponding to the (002) plane of graphite (PDF No. 13-0148). Notably, this peak in the GF/NiSA-P electrode is weaker and shifts towards the lower angle, indicating the increase of interlayer spacing within the graphitic structure owing to the formation of graphite foam [24]. Additionally, no diffraction peaks for Ni are identified in the GF/NiSA-P electrode, ruling out the formation of large Ni nanoparticles. Raman spectra of CGP and the as-resulted samples are illustrated in Figure S6, similar spectral features suggest the retained graphitic framework with excellent electrical conductivity for the GF/NiSA-P

absorption spectroscopy (XAS) were conducted to probe the electronic structures of the resulting samples. As shown in Figure S7a-c, all samples exhibit distinct C 1s XPS peaks along with weaker O 2p XPS peaks. However, no significant Ni 2p signal is detected in the GF/NiSA-P electrode, as further confirmed by the high-resolution Ni 2p XPS spectrum in Figure S7d. The absence of Ni 2p XPS peak could be attributed to the ultralow content of Ni, which is approximately 0.07 wt.% as determined by inductively coupled plasma-mass spectrometry (ICP-MS) measurement.

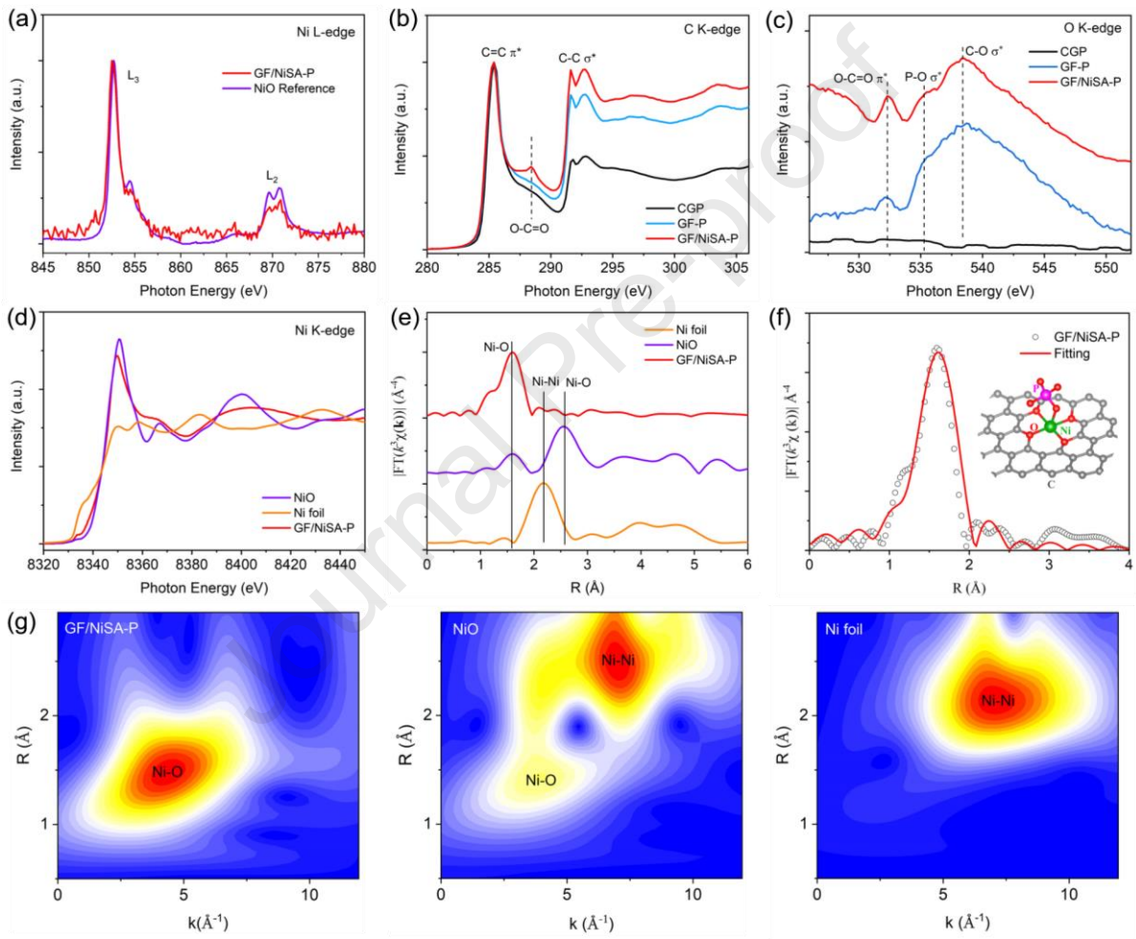

Figure 3. (a) Ni L-edge XAS, (b) C K-edge XAS, and (c) O K-edge XAS of different samples; (d) Ni K-edge XANES and (e) EXAFS spectra of GF/NiSA-P and standard samples (Ni foil and NiO); (f) EXAFS fitting of GF/NiSA-P in R space (inset: optimized coordination environment of Ni atom), (g) Ni K-edge WT-EXAFS contour plots of GF/NiSA-P and standard samples (Ni foil and NiO).

Figure 3a presents the Ni L-edge XAS of the GF/NiSA-P electrode, two groups of typical peaks are observed at approximately 852.5 eV (L_3-edge) and 870.3 eV (L_2-edge),

corresponding to the splitting of the Ni 2p orbitals [36]. Moreover, these spectral features resemble those of the NiO reference, indicating that in the GF/NiSA-P electrode, the Ni atoms are mainly coordinated with O atoms from the oxidized functional species within the CQDs. As depicted in Figure 3b, the C K-edge XAS demonstrates a distinct peak centered at ~288.4 eV in the GF/NiSA-P electrode while it is absent in CGP and GF-P samples. This peak can be attributed to oxygen-containing carboxylic (O-C=O) groups [33,37], originating from the decomposition of the Ni-HEDP complex. Figure 3c illustrates the O K-edge XAS for CGP, GF-P, and GF/NiSA-P samples. Both the GF-P and GF/NiSA-P samples exhibit a peak around 532.3 eV associated with carboxylic groups, along with a C-O σ* bonding feature at ~540 eV [38]. Notably, the peak intensity of carboxylic groups of the GF/NiSA-P electrode is stronger than that of the GF-P sample, suggesting a higher content of O-C=O groups. All these observations indicate a substantial presence of oxidized functional groups on the CQDs surface in the GF/NiSA-P electrode, which likely act as the planar coordination structure to bond to the atomically dispersed Ni atoms. Moreover, the O K-edge XAS has revealed additional peaks around 535.5 eV in both GF-P and GF/NiSA-P samples, corresponding to P-O bonds from the pyrolysis of HEDP and Ni-HEDP complex, respectively [39]. This finding is further affirmed by high-resolution O 1s XPS spectra (Figure S7c), where the P-O bonds could be detected in GF-P and GF/NiSA-P samples. Figure S7e illustrates the high-resolution P 2p XPS spectra for the GF-P and GF/NiSA-P samples, a predominate peak at around 133.5 eV in the GF-P sample corresponds to C-P-O_3/C_2-PO_2 bonds [40,41], i.e., P species are mainly bonded with carbon atoms in the graphite foam. In contrast, the P 2p XPS peak for the GF/NiSA-P electrode shows a higher binding energy of ~134 eV, attributed to highly oxidized P atoms in PO_4^{3-}. The different states of P atoms in the GF-P and GF/NiSA-P samples indicate that P atoms in the GF/NiSA-P sample do not bond with carbon but are likely axially coordinated with atomically dispersed Ni atoms (Ni-O-PO_3) [41,42]. The presence of oxidized P groups in the GF/NiSA-P electrode is further confirmed by P L-edge XAS (Figure S7f), which displays a peak at ~ 136.5 eV, resulting from the 1s to π* transition of P=O of phosphate groups [43]. All these results strongly suggest that the P element in the GF/NiSA-P electrode mainly exists as the axial PO_4 coordination with atomically dispersed Ni atoms.

X-ray absorption near-edge structure (XANES) and extended X-ray absorption fine structure (EXAFS) at the Ni K-edge of the GF/NiSA-P electrode were conducted to explore the coordination structure of atomically dispersed Ni atoms in more detail. As illustrated in Figure 3d, the XANES spectra show that the absorption edge position of the GF/NiSA-P electrode is closer to that of NiO reference, suggesting that the valence state of Ni atoms in the GF/NiSA-P electrode is +2, identical to the Ni L-edge XAS spectra. Figure 3e shows the EXAFS spectra of samples, where the GF/NiSA-P electrode exhibits a prominent peak at about 1.60 Å, resembling the Ni-O coordination observed in the NiO reference. Moreover, no peak corresponding to the Ni-Ni bond at around 2.18 Å is detected, indicating the atomic dispersion of oxygen-bonded Ni in the GF/NiSA-P. This is further evidenced by the EXAFS wavelet transform (WT) shown in Figure 3g, which demonstrates an intensity maximum corresponding to the Ni-O bond and the absence of the Ni-Ni bond in the GF/NiSA-P electrode. Further, EXAFS data fitting in R space was carried out to accurately quantify the structural configuration of Ni-O coordination in the GF/NiSA-P electrode [44]. As presented in Table S1, the fitting results indicate a coordination number (CN) of 5.3 for Ni-O bonds, suggesting that the atomically dispersed Ni atoms are coordinated with four in-plane oxygen atoms from O-PO_3 ligands (Ni-O_4(O-PO_3)), as shown in the insert of Figure 3f.

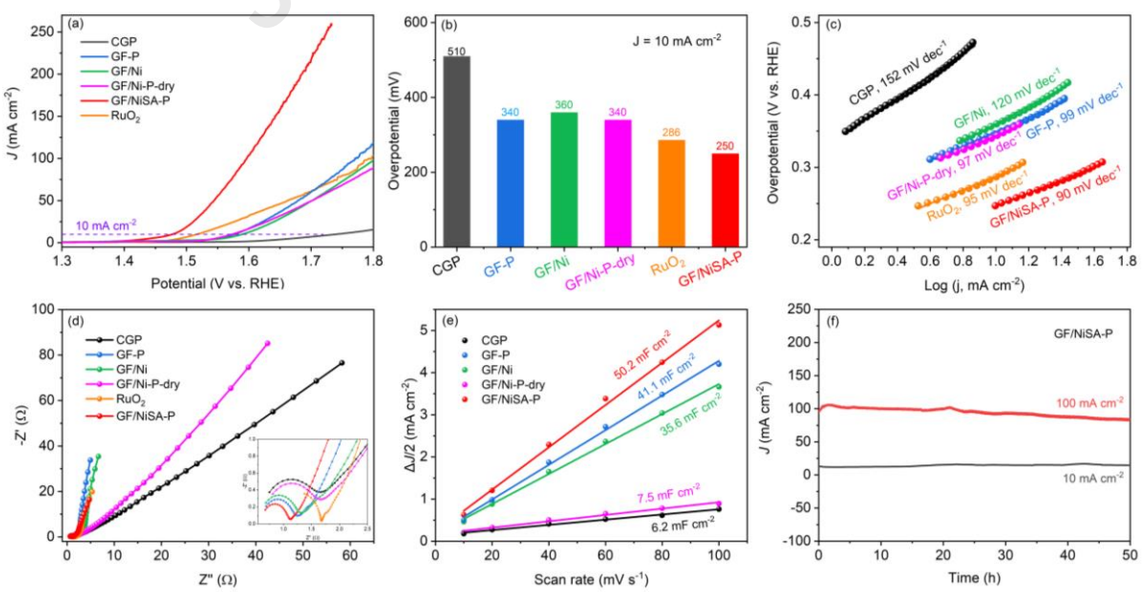

Figure 4. (a) The OER polarization profiles, (b) the overpotentials at 10 mA cm^{-2}, (c) the corresponding Tafel plots, (d) EIS spectra, (e) the capacitive current density at about 1.18 V vs. RHE against the scan rate, and (f) the durability curves of as-resulted samples.

The OER performance of the resulting samples was evaluated in a standard three-electrode system using an alkaline electrolyte. Figure S8 displays the linear sweep voltammetry (LSV) plots of GF/NiSA-P electrodes fabricated with different input current densities (100-160 A) and duration time (0.3-5 s) for the flash Joule heating as well as various concentrations (0.03-0.06 M) of $NiCl_6$ in Ni-HEDP precursor solution, demonstrating that the sample fabricated at 130 A and 0.5 s for flash Joule heating and 0.05 M for $NiCl_6$ precursor exhibits the optimal OER activity. As shown in Figure 4a and Figure 4b, this optimal sample requires a low overpotential (η_{10}) of 250 mV to afford a current density of 10 mA cm^{-2}, outperforming CGP (510 mV), GF/Ni (360 mV), GF-P (340 mV), GF/Ni-P-dry (340 mV), and commercial RuO_2 (286 mV). The remarkable OER activity of the GF/NiSA-P electrode is further confirmed by Tafel curves. Figure 4c shows that the GF/NiSA-P electrode has the smallest slope of 90 mV dec^{-1} compared to CGP (152 mV dec^{-1}), GF-P (99 mV dec^{-1}), GF/Ni (120 mV dec^{-1}), GF/Ni-P-dry (97 mV dec^{-1}), and commercial RuO_2 (95 mV dec^{-1}) samples, implying the fastest OER kinetics. Notably, the overpotential and kinetics of the GF/NiSA-P electrode are comparable with the most active Ni-based OER catalysts reported (Table S2), highlighting its exceptional OER performance. Electrochemical impedance spectroscopy (EIS) measurements were subsequently conducted to investigate the charge transfer properties of the resulting samples. As depicted in Figure 4d, the Nyquist plots recorded at an open circuit potential show that the GF/NiSA-P electrode exhibits the smallest arc radius, suggesting that the combination of graphite foam formation and atomically dispersed Ni atoms anchoring effectively improves charge transfer kinetics. On the other hand, the porous structure of catalysts has been known to significantly boost the OER activity by offering more catalytic active sites via increasing the electrochemically active surface area (ECSA) [45]. Consequently, ECSA was evaluated by obtaining the double-layer capacitance (C_{dl}) from cyclic voltammogram (CV) measurement in a non-faradic window (Figure S9). Figure 4e illustrates the resulting C_{dl} values, it is clear that the GF/NiSA-P electrode exhibits a drastically improved value of 50.2 mF cm^{-2}, approximately

8.1 and 1.2 times higher than those of CGP and GF-P samples, respectively. This implies a significantly increased ECSA for the GF/NiSA-P electrode, i.e., providing a larger concentration of active sites and thereby enhancing OER activity.

Durability is crucial for the practical application of electrocatalysts, therefore the durability of the GF/NiSA-P electrode was assessed. As presented in Figure 4f, the chronoamperometry (CA; applied potential-time) curve reveals that there are no significant attenuations in the current densities of 10 and 100 mA cm^{-2} after continuous OER operation for 50 hours, suggesting promising durability and it is most likely due to the 3D porous skeleton structure of the graphite foam [46,47]. Additionally, Figure S10 demonstrates that the LSV curve of the GF/NiSA-P electrode after 2000 CV scans nearly overlaps with the curve after 1000 CV scans, with only slight degradation compared to the initial performance. These results indicate the synergistic effects of the graphite foam and anchored atomically dispersed Ni atoms in promoting OER activity and durability. The 3D graphite foam not only significantly increases the contact area between the electrolyte and the electrode for facilitating both interfacial electron transfer and mass transport but also serves as a stable skeleton for the long-term water oxidation reaction. Simultaneously, the atomically dispersed Ni atoms contribute catalytic activate sites for the OER process.

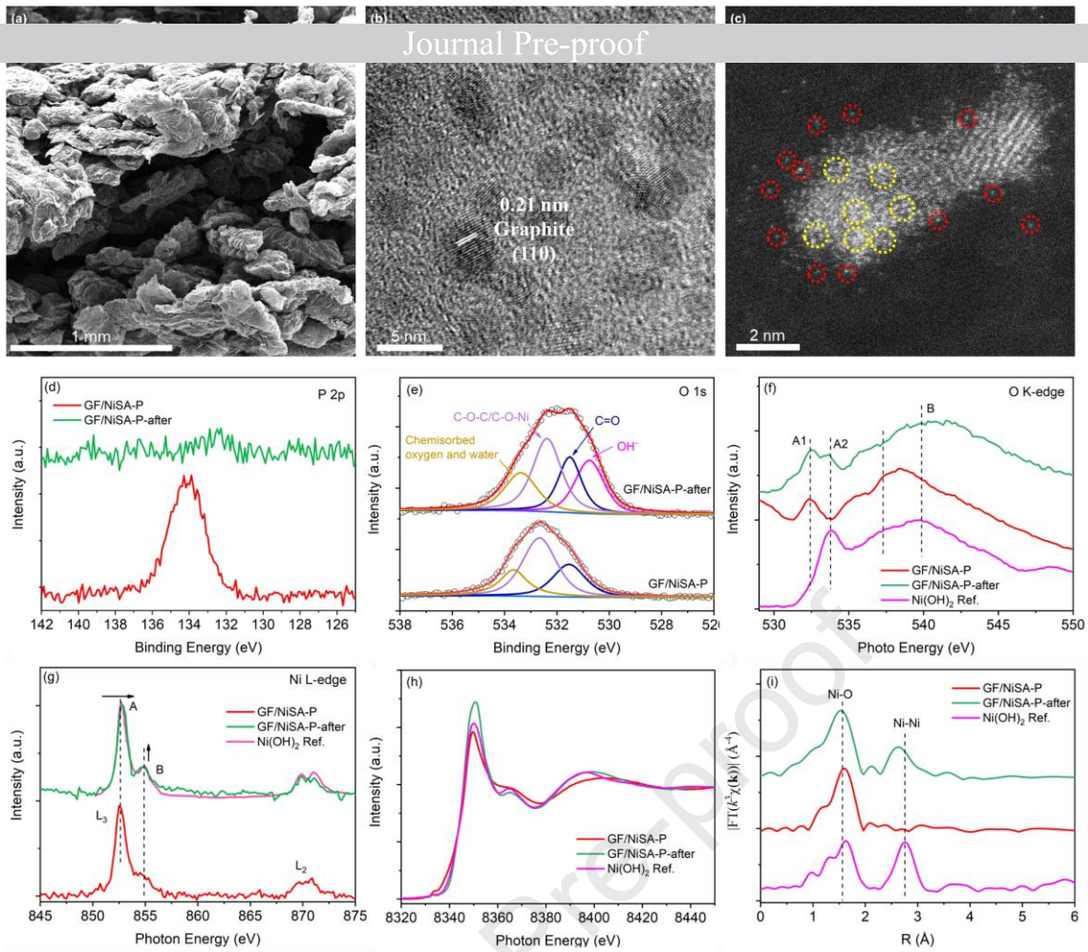

Figure 5. (a) SEM image, (b) HRTEM image, and (c) STEM image of GF/NiSA-P electrode after CV activation; (d) P 2p XPS spectra, (e) O 1s XPS spectra, (f) O K-edge XAS spectra, (g) Ni L-edge XAS spectra, (h) Ni K-edge XANES spectra, and (i) EXAFS spectra for GF/NiSA-P before and after CV activation.

To understand the catalytic mechanism of the GF/NiSA-P electrode, SEM, TEM, STEM, XPS, and XAS characterizations were conducted to investigate the structural evolution of GF/NiSA-P during the OER reaction. As shown in SEM images in Figure 5a and Figure S11, the microstructure of worm-like strips, composed of crumpled graphene-liked nanosheets, is well preserved after CV activation. Additionally, no large nanoparticles are observed on the smooth surface of graphene-like nanosheets. Figure S12 and Figure 5b display the HRTEM images of the GF/NiSA-P electrode after CV activation (labeled as GF/NiSA-P-after), revealing abundant graphite carbon dots with clear lattices on the surface of graphene-like carbon nanosheets. All these are indicative of the high chemical stability of graphitic carbon in an alkaline environment and are further supported by the good crystallinity of the GF/NiSA-P electrode after CV tests (XRD patterns in Figure S13). On the other hand, the surface

reconstruction of SAC and metal phosphates during OER reaction has been widely reported [48-50]. Therefore, XPS and XAS measurements were conducted to explore the real active centers of GF/NiSA-P for the OER. As shown in Figure S14, the high corrosion resistance of graphitic carbon results in negligible differences in the C 1s XPS and C K-edge XAS spectra for the sample before and after OER activation. In contrast, after activation, the P 2p XPS peak nearly vanishes (Figure 5d) while the O 1s XPS peak significantly increases (Figure 5e), suggesting a decrease in the content of phosphate ligands, likely due to anion exchange from PO_4^{3-} to OH^- during activation [51]. Moreover, Figure 5e shows a prominent peak at 530.7 eV in the O 1s XPS spectrum for the GF/NiSA-P-after sample, indicating the presence of oxy/hydroxides groups [52,53], further corroborated by O K-edge and Ni L-edge XAS. In the O K-edge XAS in Figure 5f, the peak corresponding to the P-O bond (~535.eV) in the GF/NiSA-P sample disappears after activation. Meanwhile, a new peak A2 around 533.8 eV and the main peak B at 540 eV are observed in the GF/NiSA-P-after sample, attributed to oxy/hydroxide species when compared to $Ni(OH)_2$ reference [54,55]. Figure 5g presents the Ni L-edge XAS, in which the GF/NiSA-P-after sample shows a higher energy shift in peak A and increased intensity in peak B, resembling the spectrum features of $Ni(OH)_2$ reference, further demonstrating the formation of oxy/hydroxide groups [54,55]. In summary, XPS and soft XAS results confirm the reconstruction of P ligands in the GF/NiSA-P sample into oxy/hydroxide species during activation. Further, Ni K-edge XANES and EXAFS characterizations were performed to probe the evolution of the local environment of atomically dispersed Ni sites during activation. As displayed in Figure 5h, the XANES spectrum of GF/NiSA-P-after sample exhibits features similar to those of $Ni(OH)_2$ reference, indicating the generation of oxy/hydroxide groups from the CV activation. Figure 5i shows the EXAFS spectra of the GF/NiSA-P sample before and after activation, clearly demonstrating a new scattering of Ni-Ni at ~2.6 Å in the GF/NiSA-P-after sample, aligning well with $Ni(OH)_2$ reference. It is indicative of the coexistence of atomically dispersed Ni-OH sites and $Ni(OH)_2$ clusters in the GF/NiSA-P-after sample. Figure 5c presents the HAADF-STEM image of the GF/NiSA-P-after electrode, offering more evidence of the co-existence of isolated Ni atoms (circled in red color) and the smaller $Ni(OH)_2$ clusters (circled in yellow color). These results

suggest that after CV activation, the P ligands of atomically distributed Ni atoms undergo a transformation into oxy/hydroxide groups, and simultaneously the isolated Ni atoms are partially agglomerated into very small $Ni(OH)_2$ clusters due to the applied potential, which then serve as the real active sites for catalyzing the OER [48,56].

4. Conclusions

A self-supporting electrode composed of a three-dimensional (3D) graphene foam integrated with axial phosphate-coordinated atomically dispersed Ni atoms was fabricated using a wet-interfacial flash Joule heating approach in just 400 milliseconds. The high conductivity and large surface area of the 3D graphene foam effectively facilitate electron and proton transport in the OER process. Furthermore, during activation, the axially coordinated phosphate ligands on the atomically dispersed Ni site induce an in-situ reconstruction into isolated Ni-OH sites and small $Ni(OH)_2$ clusters, thereby accelerating the OER kinetics. As a result of these synergistic effects, the resulting electrode achieves a low overpotential of 250 mV to reach a current density of 10 mA cm^{-2} and demonstrates excellent long-term durability. This study introduces an innovative approach for the ultrafast preparation of a self-supporting electrode by anchoring atomic catalysts onto 3D carbon foam, highlighting significant benefits in simplicity, efficiency, and cost-effectiveness.

ASSOCIATED CONTENT

Supporting Information. The Supporting Information is available free of charge at http://XXXX. Experimental setup, Heating/quenching curve, XRD patterns, XAS spectra, XPS spectra, SEM images, TEM images, Raman spectra, LSV curves, and CV plots.

AUTHOR INFORMATION

Author Contributions

All authors have given approval to the final version of the manuscript.

Notes

The authors declare no competing financial interest.

ACKNOWLEDGMENTS

We acknowledge the financial support from the Scientific Research Startup Foundation of Jiangsu University (18JDG019) and the National Natural Science Foundation of China (22208126). We acknowledge the support from the Beijing Synchrotron Radiation Facility (BSRF) and National Synchrotron Radiation Laboratory (NSRL, Beamlines MCD-A and MCD-B (Soochow Beamline for Energy Materials)) for the XAS experiments.

REFERENCES:

[1] B. You, Y. Sun, Innovative Strategies for Electrocatalytic Water Splitting, Acc. Chem. Res. 51 (2018) 1571-1580.

[2] J. Song, C. Wei, Z.-F. Huang, C. Liu, L. Zeng, X. Wang, et al., A Review on Fundamentals for Designing Oxygen Evolution Electrocatalysts, Chem. Soc. Rev. 49 (2020) 2196-2214.

[3] L. Du, L. Xing, G. Zhang, S. Sun, Metal-Organic Framework Derived Carbon Materials for Electrocatalytic Oxygen Reactions: Recent Progress and Future Perspectives, Carbon 156 (2020) 77-92.

[4] J. Liang, H. Li, L. Chen, M. Ren, O. A. Fakayode, J. Han, et al., Efficient Hydrogen Evolution Reaction Performance Using Lignin-Assisted Chestnut Shell Carbon-Loaded Molybdenum Disulfide, Ind. Crops Prod. 193 (2023) 116214.

[5] Q. Wang, Y. Cheng, H. B. Tao, Y. Liu, X. Ma, D.-S. Li, et al., Long-Term Stability Challenges and Opportunities in Acidic Oxygen Evolution Electrocatalysis, Angew. Chem., Int. Ed. 62 (2023) e202216645.

[6] Z. Li, X. Zhang, C. Ou, Y. Zhang, W. Wang, S. Dong, et al., Transition Metal-Based Self-Supported Anode for Electrocatalytic Water Splitting at A Large Current Density, Coord. Chem. Rev. 495 (2023) 215381.

[7] J. Hao, K. Wu, C. Lyu, Y. Yang, H. Wu, L. Liu, et al., Recent Advances in Interface Engineering of Fe/Co/Ni-Based Heterostructure Electrocatalysts for Water Splitting, Mater. Horiz. 10 (2023) 2312-2342.

[8] A. Wang, J. Li, T. Zhang, Heterogeneous Single-Atom Catalysis, Nat. Rev. Chem. 2 (2018) 65-81.

[9] S. E. Jun, S. Choi, J. Kim, K. C. Kwon, S. H. Park, H. W. Jang, Non-Noble Metal Single Atom Catalysts for Electrochemical Energy Conversion Reactions, Chin. J. Catal. 50 (2023) 195.

[10] Y. Wang, X. Cui, J. Zhang, J. Qiao, H. Huang, J. Shi, et al., Advances of Atomically Dispersed Catalysts from Single-Atom to Clusters in Energy Storage and Conversion Applications, Prog. Mater. Sci. 128 (2022) 100964.

[11] H. Sun, Z. Yan, F. Liu, W. Xu, F. Cheng, J. Chen, Self-Supported Transition-Metal-Based Electrocatalysts for Hydrogen and Oxygen Evolution, Adv. Mater. 32 (2020) 1806326.

[12] M. N. Hossain, L. Zhang, R. Neagu, E. Rassachack, Free-Standing Single-Atom Catalyst-Based Electrodes for CO_2 Reduction, Electrochem. Energy Rev. 7 (2024) 5.

[13] X. Zheng, P. Li, S. Dou, W. Sun, H. Pan, D. Wang, et al., Non-Carbon-Supported Single-Atom Site Catalysts for Electrocatalysis, Energy Environ. Sci. 14 (2021) 2809-2858.

[14] Z. Li, B. Li, C. Yu, Atomic Aerogel Materials (or Single-Atom Aerogels): An Interesting New Paradigm in Materials Science and Catalysis Science, Adv. Mater. 35 (2023) 2211221.

[15] T. Y. Ma, S. Dai, S. Z. Qiao, Self-Supported Electrocatalysts for Advanced Energy Conversion Processes, Mater. Today 19 (2016) 265-273.

[16] L. Zhang, N. Jin, Y. Yang, X.-Y. Miao, H. Wang, J. Luo, et al., Advances on Axial Coordination Design of Single-Atom Catalysts for Energy Electrocatalysis: A Review, Nano-Micro Lett. 15 (2023) 228.

[17] X. Liu, Y. Liu, W. Yang, X. Feng, B. Wang, Controlled Modification of Axial Coordination for Transition-Metal Single-Atom Electrocatalyst, Chem. Eur. J. 28 (2022) e202201471.

[18] Q. Deng, J. Zhao, T. Wu, G. Chen, H. A. Hansen, T. Vegge, 2D Transition Metal-TCNQ Sheets as Bifunctional Single-Atom Catalysts for Oxygen Reduction and Evolution Reaction (ORR/OER), J. Catal. 370 (2019) 378-384.

[19] H. Su, S. Song, N. Li, Y. Gao, P. Li, L. Ge, et al., Flexibility Tuning of Dual-Metal Sₐ-Fe-Co-N$_5$ Catalysts with O-Axial Ligand Structure for Electrocatalytic Water Splitting, Adv. Energy Mater. 13 (2023) 2301547.

[20] T. Liu, Y. Wang, Y. Li, Two-Dimensional Organometallic Frameworks with Pyridinic Single-Metal-Atom Sites for Bifunctional ORR/OER, Adv. Funct. Mater. 32 (2022) 2207110.

[21] T. Zhang, D. Yuan, Q. Guo, F. Qiu, D. Yang, Z. Ou, Preparation of a Renewable Biomass Carbon Aerogel Reinforced with Sisal for Oil Spillage Clean-Up: Inspired by Green Leaves to Green Tofu, Food Bioprod. Process. 114 (2019) 154-162.

[22] L. Wu, W. Li, P. Li, S. Liao, S. Qiu, M. Chen, et al., Powder, Paper and Foam of Few-Layer Graphene Prepared in High Yield by Electrochemical Intercalation Exfoliation of Expanded Graphite, Small 10 (2014) 1421-1429.

[23] L. Chen, Y. Li, J. Yao, G. Wu, B. Yang, L. Lei, et al., Fast Expansion of Graphite into Superior Three-Dimensional Anode for Microbial Fuel Cells, J. Power Sources 412 (2019) 86-92.

[24] Y. Z. N. Htwe, W. S. Chow, Y. Suda, A. A. Thant, M. Mariatti, Effect of Electrolytes and Sonication Times on The Formation of Graphene Using an Electrochemical Exfoliation Process, Appl. Surf. Sci. 469 (2019) 951.

[25] H. Fei, J. Dong, C. Wan, Z. Zhao, X. Xu, Z. Lin, et al., Microwave-Assisted Rapid Synthesis of Graphene-Supported Single Atomic Metals, Adv. Mater. 30 (2018) 1802146.

[26] L. Xing, R. Liu, Z. Gong, J. Liu, J. Liu, H. Gong, et al., Ultrafast Joule Heating Synthesis of Hierarchically Porous Graphene-Based Co-N-C Single-Atom Monoliths, Nano Res. 15 (2022) 3913-3919.

[27] G. He, M. Yan, H. Gong, H. Fei, S. Wang, Ultrafast Synthetic Strategies under Extreme Heating Conditions Toward Single-Atom Catalysts, Int. J. Extrem. Manuf. 4 (2022) 032003.

[28] Y. Yao, Z. Huang, P. Xie, L. Wu, L. Ma, T. Li, et al., High Temperature Shockwave Stabilized Single Atoms, Nat. Nanotechnol. 14 (2019) 851-857.

[29] D. Xi, J. Li, J. Low, K. Mao, P. Long, J. Li, et al., Limiting the Unsaturated N Species in M-N_x Single-Atom Catalysts toward Electrocatalytic CO_2 Reduction in Broad Voltage Range, Adv. Mater. 34 (2022) 2104090.

[30] D. Jiang, Y. Yao, T. Li, G. Wan, X. I. Pereira-Hernández, Y. Lu, et al., Tailoring the Local Environment of Platinum in Single-Atom Pt_1/CeO_2 Catalysts for Robust Low-Temperature CO Oxidation, Angew. Chem., Int. Ed. 60 (2021) 26054-26062.

[31] L. Zhang, L. Peng, Y. Lu, X. Ming, Y. Sun, X. Xu, et al., Sub-Second Ultrafast Yet Programmable Wet-Chemical Synthesis, Nat. Commun. 14 (2023) 5015.

[32] X. Cui, Y. Liu, X. Wang, X. Tian, Y. Wang, G. Zhang, et al., Rapid High-Temperature Liquid Shock Synthesis of High-Entropy Alloys for Hydrogen Evolution Reaction, ACS Nano 18 (2024) 2948-2957.

[33] G. Li, W. Zhang, K. Nie, X. Lv, J. Deng, H. Ji, Flash Joule Heating to Enhance Water Oxidation of Hematite Photoanode via Mediating with an Oxidized Carbon Overlayer, Carbon 215 (2023) 118444.

[34] J. Deng, G. Li, D. Yan, W. Zhang, K. Feng, K. Nie, et al., Programmable Wet-Interfacial Joule Heating to Rapidly Synthesize Metastable Protohematite Photoanodes: Metal and Lattice Oxygen Dual Sites for Improving Water Oxidation, ACS Catal. 14 (2024) 10635-10647.

[35] Y. He, C. Zhen, M. Li, X. Wei, C. Li, Y. Zhu, et al., Differing Electrolyte Implication on Anion and Cation Intercalation into Graphite, ACS Nano 17 (2023) 21730-21738.

[36] Y. Cheng, S. Zhao, H. Li, S. He, J.-P. Veder, B. Johannessen, et al., Unsaturated Edge-Anchored Ni Single Atoms on Porous Microwave Exfoliated Graphene Oxide for Electrochemical CO_2, Appl. Catal., B 243 (2019) 294-303.

[37] J. Zhong, H. Zhang, X. Sun, S.-T. Lee, Synchrotron Soft X-ray Absorption Spectroscopy Study of Carbon and Silicon Nanostructures for Energy Applications, Adv. Mater. 26 (2014) 7786-7806.

[38] J. Zhou, Y. Hu, X. Li, C. Wang, L. Zuin, Chemical Bonding in Amorphous Si-Coated Carbon Nanotubes as Anodes for Li Ion Batteries: A XANES Study, RSC Adv. 4 (2014) 20226-20229.

[39] S. O. Kucheyev, C. Bostedt, T. van Buuren, T. M. Willey, T. A. Land, L. J. Terminello, et al., Electronic Structure of $KD_{2x}H_{2(1-x)}PO_4$ Studied by Soft X-Ray Absorption and Emission Spectroscopies, Phys. Rev. B 70 (2004) 245106.

[40] Y. Liu, K. Li, Y. Liu, L. Pu, Z. Chen, S. Deng, The High-Performance and Mechanism of P-Doped Activated Carbon as A Catalyst for Air-Cathode Microbial Fuel Cells, J. Mater. Chem. A 3 (2015) 21149-21158.

[41] N. Rey-Raap, M. A. C. Granja, M. F. R. Pereira, J. L. Figueiredo, Phosphorus-Doped Carbon/Carbon Nanotube Hybrids as High-Performance Electrodes for Supercapacitors, Electrochim. Acta 354 (2020) 136713.

[42] Y. Liu, S. Zhang, C. Jiao, H. Chen, G. Wang, W. Wu, et al., Axial Phosphate Coordination in Co Single Atoms Boosts Electrochemical Oxygen Evolution, Adv. Sci. 10 (2023) 2206107.

[43] X. Zhu, X. Tan, K.-H. Wu, C.-L. Chiang, Y.-C. Lin, Y.-G. Lin, et al., N, P Co-Coordinated Fe Species Embedded in Carbon Hollow Spheres for Oxygen Electrocatalysis, J. Mater. Chem. A 7 (2019) 14732-14742.

[44] Y. G. Li, Z.-S. Wu, P. F. Lu, X. Wang, W. Liu, Z. B. Liu, et al., High-Valence Nickel Single-Atom Catalysts Coordinated to Oxygen Sites for Extraordinarily Activating Oxygen Evolution Reaction, Adv. Sci. 7 (2020) 1903089.

[45] S. Oh, H. Kim, Y. Kwon, M. Kim, E. Cho, H. Kwon, Porous Co-P Foam as An Efficient Bifunctional Electrocatalyst for Hydrogen and Oxygen Evolution Reactions, J. Mater. Chem. A 4 (2016) 18272-18277.

[46] X. Yu, M. Zhang, J. Chen, Y. Li, G. Shi, Nitrogen and Sulfur Codoped Graphite Foam as a Self-Supported Metal-Free Electrocatalytic Electrode for Water Oxidation, Adv. Energy Mater. 6 (2016) 1501492.

[47] M. P. Suryawanshi, U. V. Ghorpade, S. W. Shin, U. P. Suryawanshi, E. Jo, J. H. Kim, Hierarchically Coupled Ni:FeOOH Nanosheets on 3D N-Doped Graphite Foam as Self-Supported Electrocatalysts for Efficient and Durable Water Oxidation, ACS Catal. 9 (2019) 5025-5034.

[48] S. Lv, Z. Zhang, C. Cheng, B. Zhang, Y. Shi, Unveiling the Aggregation of M-N-C Single Atom Electrocatalysts into Highly Efficient MOOH Nanoclusters during Alkaline Water Oxidation, Angew. Chem., Int. Ed. 64 (2024) e202413308.

[49] J. Cai, X. Hao, Z. Bian, Y. Wu, C. Wei, X. Yin, et al., Elucidating the Discrepancy between the Intrinsic Structural Instability and the Apparent Catalytic Steadiness of M-N-C Catalysts toward Oxygen Evolution Reaction, Angew. Chem., Int. Ed. 63 (2024) e202409079.

[50] S. Shao, Y. Xiao, J. Yang, X. Lv, K. Feng, Y. Xia, et al., In-Situ Surface Reconstruction in Pt and P Co-Treated Hematite for Enhanced Water Oxidation, Chem. Eng. J. 413 (2021) 127416.

[51] R. Duan, Y. Li, S. Wang, J. Gong, Y. Tong, W. Qi, Fast and Deep Reconstruction of Coprecipitated Fe Phosphates on Nickel Foams for an Alkaline Oxygen Evolution Reaction, J. Phys. Chem. Lett. 13 (2022) 1446-1452.

[52] A. Indra, U. Paik, T. Song, Boosting Electrochemical Water Oxidation with Metal Hydroxide Carbonate Templated Prussian Blue Analogues, Angew. Chem., Int. Ed. 57 (2018) 1241.

[53] A. De, A. Karmakar, S. Kundu, Enhancing the Surface-Active Sites of Bimetallic 2D Hydroxide Materials by Introducing Fe^{2+} Ions toward Effective Hydroxide Adsorption for the Water Oxidation Reaction, ACS Appl. Energy Mater. 6 (2023) 5761-5773.

[54] S. Tao, G. Zhang, B. Qian, J. Yang, S. Chu, C. Sun, et al., Spectroscopically Unraveling High-Valence Ni-Fe Catalytic Synergism in $NiSe_2/FeSe_2$ Heterostructure, Appl. Catal., B 330 (2023) 122600.

[55] G. E. Yalovega, M. Brzhezinskaya, V. O. Dmitriev, V. A. Shmatko, I. V. Ershov, A. A. Ulyankina, et al., Interfacial Interaction in MeO_x/MWNTs (Me-Cu, Ni) Nanostructures as Efficient Electrode Materials for High-Performance Supercapacitors, Nanomaterials 14 (2024) 947.

[56] M. Hou, L. Zheng, D. Zhao, X. Tan, W. Feng, J. Fu, et al., Microenvironment Reconstitution of Highly Active Ni Single Atoms on Oxygen-Incorporated Mo_2C for Water Splitting, Nat. Commun. 15 (2024) 1342.

Declaration of interests

☒ The authors declare that they have no known competing financial interests or personal relationships that could have appeared to influence the work reported in this paper.

☐ The authors declare the following financial interests/personal relationships which may be considered as potential competing interests: